Regional-scale, high-resolution measurements of hilltop curvature reveal tectonic, climatic, and lithologic controls on hillslope morphology

William T. Struble[1,2,3], Fiona J. Clubb[4], Joshua J. Roering[2]

[1]Department of Geosciences, University of Arizona, Tucson, AZ, USA
[2]Department of Earth Sciences, University of Oregon, Eugene, OR, USA
[3]Now at Department of Earth & Atmospheric Sciences, University of Houston, Houston, TX
[4]Department of Geography, Durham University, Durham, UK

Correspondence to: William T. Struble (wstruble@uh.edu)

Key words: geomorphology, hillslopes, hilltop curvature, erosion, tectonics, climate

Abstract.

Climate, tectonics, lithology, and biology are encoded within the morphology of landforms. Hillslopes record uplift and erosion rate through hilltop curvature, in which sharper, more convex hilltops correspond with more rapid erosion rates. However, past hilltop curvature studies that map uplift and erosion rates have been limited to small spatial scales largely due to relatively slow speeds of curvature measurement techniques. This lack of regional-scale observations has made deconvolving the relative contributions of tectonics, climate, and lithology to hillslope morphology a challenge. Here, we used high performance computing and continuous wavelet transforms of topography to rapidly map hilltop curvature in the steep and dissected Oregon Coast Range (OCR) and the adjacent gentler Cascadia Forearc Lowland (CFL) in western Oregon, amounting to ~43,000 km^2 of 1-meter lidar data. We additionally compared mapped hilltop curvature to published erosion rates derived from cosmogenic ^{10}Be, including 11 newly sampled watersheds. We observed that hilltops are systematically sharper in the OCR than in the CFL, and we noted a linear relationship between catchment-averaged erosion rate

and hilltop curvature, consistent with previous observations and theory that erosion rate scales linearly with hilltop curvature in soil-mantled landscapes. The boundary between the OCR and CFL, as demarcated by hilltop curvature, is often abrupt and occurs across mapped structures that separate disparate baselevels but where lithology and mean annual precipitation remain constant. Thus, while we observed significant variability in hilltop curvature that results from secondary lithologic and climatic controls, our results demonstrate that hillslope morphology in western Oregon is set primarily by uplift via tectonically-controlled baselevel lowering rates. These regional interpretations additionally highlight the computational advantages of the wavelet transform for rapidly quantifying hilltop curvature.

1 Introduction

The morphology of landforms has often been utilized as a proxy for the rate at which landscapes uplift and erode. In steady-state landscapes (i.e., uplift equals erosion) the steepness of bedrock river channels has been noted to correlate with uplift rate, wherein watersheds experiencing rapid uplift exhibit systematically steeper channels than more slowly uplifting watersheds (Kirby and Whipple, 2001). As such, channel steepness is the most widely used metric to infer uplift and erosion rate across landscapes, especially since rivers often span tectono-climatic regimes, allowing them to continuously record climate and tectonics in space and time over regional scales (Adams et al., 2020; DiBiase et al., 2010). Furthermore, quantitative analysis of river network geometry, including steepness and integrated measurements of drainage area (i.e., χ), is commonly used to infer regional scale planform drainage reorganization (Willett et al., 2014). However, the spatial connectivity of river networks means that signals from uplift, climate, sediment supply, and other exogenic processes are often integrated into morphology throughout the river network (Lai et al., 2021; Willett et al., 2014), thus complicating local process interpretations. In addition, bedrock channels compose only a small fraction of landscapes, while hillslopes comprise a significant proportion of landscape relief and the majority of landscape area.

It has long been recognized that hillslopes record rates of baselevel fall (Gilbert, 1877), although they have been a comparatively underutilized landform for mapping uplift and erosion rate. For instance, the gradient and convexity of hillslopes serve as useful proxies of erosion rate (Gilbert, 1877), similar to bedrock-river metrics like channel steepness (DiBiase et al., 2010). Field and experimental observations support a linear relationship between hillslope sediment flux and gradient in many gentle, slowly eroding landscapes (Culling, 1963). In steep landscapes, however, hillslope gradient becomes decoupled from erosion rate and approaches a threshold value as shallow landslides and granular creep become more common and accelerate (Deshpande et al., 2021; Larsen and Montgomery, 2012; Roering et al., 1999), making hillslope gradient an ineffective morphologic proxy at fast erosion rates. However, as erosion rate increases, the convexity of soil-mantled hilltops maintains a linear relationship with erosion rate, even as slopes between the hilltop and bounding channel reach a threshold angle (Hurst et al., 2012; Roering et al., 2007). Specifically, erosion rate, E, varies with hilltop curvature, C_{HT}, expressed by

$$E = -\frac{\rho_s}{\rho_r} D C_{HT}, \qquad (1)$$

where ρ_s and ρ_r are the density of soil and bedrock, respectively, and D is a soil transport coefficient, or "diffusivity." Equation 1 shows that sharp hilltops (high-magnitude curvatures) reflect more rapid erosion rates than broad, gentle hilltops (low-magnitude curvatures).

While C_{HT} is often used as a morphologic proxy for erosion rate in soil-mantled landscapes (e.g., Godard et al., 2020; Hurst et al., 2012; Roering et al., 2007; Struble and Roering, 2021), its application has generally been limited to small scales on the order of individual watersheds. This limitation has arisen largely due to the computational expense of calculating curvature and accurately identifying hilltops as well as due to a paucity of lidar data that are necessary to accurately measure C_{HT} (Grieve et al., 2016; Scherler and Schwanghart, 2020; Struble and Roering, 2021). Thus, to our knowledge, there exist no studies that examine regional-scale (>10^3 km^2) variations in C_{HT}, in contrast to fluvial metrics (e.g., χ, channel steepness), which are quite common. However, recent increases in the availability of high-resolution topographic data, including lidar, facilitates regional C_{HT} analyses, as does an increase in the computational speeds of curvature measurement techniques that have been applied to hillslope morphometric studies (Struble and Roering, 2021). Furthermore, because hillslopes are abundant relative to channels in natural landscapes, regional C_{HT} hillslope analyses will reveal landscape-scale tectonic and climatic forcings on surface processes at higher spatial resolutions than watershed-scale hillslope studies or regional river network analyses. In addition, the ability to extract local measurements of C_{HT} will permit more robust interrogation of lithologic impacts on landscape form, particularly when scaled up to larger regions and datasets.

Mapping spatial variations in C_{HT} informs efforts to constrain models and theory for how topographic form relates to surface processes boundary conditions (i.e., geomorphic transport laws, Dietrich et al., 2003). For instance, while tectonic baselevel controls on hillslope morphology are well-studied (e.g., Clubb et al., 2020; Hurst et al., 2012), the details of how lithology and climate impact hillslope form is generally poorly constrained. For instance, for the case of lithology, more resistant rocks likely support sharper hilltops, as decreased bedrock-soil conversion rates result in steeper hillslopes and/or more patchy soils in extreme cases (Heimsath et al., 2012; Hurst et al., 2013; Roering, 2008). However, trade-offs between physical and chemical weathering mechanisms, including through time (Marshall et al., 2015), may impact this hypothesized relationship as will differences in soil-production functions (i.e., exponential vs humped production curves; Dixon et al., 2009; Heimsath et al., 1997) and soil depth-dependent transport laws (e.g., Roering, 2008). Similarly, for the case of climatic controls on C_{HT}, we might expect that higher mean annual precipitation (MAP), all else equal, will produce sharper hilltops, as channels incise the base of hillslopes and increased vegetation supports steeper slopes (Perron, 2017). However, higher MAP may also correspond with greater diffusivities due primarily to increased bioturbation, thus resulting in lower C_{HT} (Perron, 2017; Richardson et al., 2019). Clearly isolating these possible relationships and constraining relative contributions of baselevel, lithology, and MAP to hillslope form has been historically hampered by the lack of regional C_{HT} analysis, largely due to a dearth of high-resolution topographic data and the computational expense of calculating curvature on those digital elevation models. As such, regional mapping of C_{HT} is invaluable not only for quantifying spatial variations in erosion rate, but also for identifying how spatial variability in climate and lithology affect hillslope morphology and, by extension, constraining how topographic form reflects heterogeneities in physical and chemical weathering, fracture generation, bioturbation, sediment transport, drainage divide migration, and soil organic carbon storage (Dixon et al., 2009; Hunter et al., 2024; Moon et al., 2017; Mudd and Furbish, 2005; Sweeney et al., 2015).

Here, we utilized continuous wavelet transforms to rapidly calculate topographic curvature in order to examine regional baselevel, climatic, and lithologic controls on C_{HT} throughout western

Oregon, a landscape that exhibits diverse uplift and erosion rates, mean annual precipitation, and rock types. We compared calculated C_{HT} to independently measured erosion rates from cosmogenic ^{10}Be for a subset of watersheds in the central Oregon Coast Range (OCR) to isolate the erosion-curvature relationship, and we additionally examined how the spatial pattern of inferred baselevel as well as mapped lithology and MAP impact the distribution of C_{HT} throughout the study area.

2. Study Area

We focused on western Oregon landscapes within the Cascadia Subduction Zone forearc, specifically the OCR and Willamette Valley (WV) as well as lowland valleys along the Umpqua and Rogue Rivers in southwestern Oregon (Figure 1). We refer to the forearc-spanning lowland that includes the WV and the Umpqua and Rogue River valleys as the Cascadia Forearc Lowland (CFL), since at long topographic wavelengths this landform spans the length of the subduction zone (Struble et al., 2021). The OCR and CFL span the Pacific Coast from near the Oregon-California border at the margin of the Klamath Mountains in the south to the Columbia River in the north (Figure 1).

Lithologic units in the southern OCR and CFL fall within the Klamath Mountains Terrane and are composed largely of early Mesozoic accreted marine and nonmarine sedimentary rocks, which are often heavily metamorphosed, as well as late Mesozoic intrusive rocks (Piotraschke et al., 2015 and references therein). The Klamath Mountains portion of our study area is primarily drained by the southern Umpqua and Rogue Rivers (Figure 1).

The central OCR is dominated primarily by two units: (1) a Paleocene-Eocene large igneous province known as Siletzia that accreted to North America ~51-49 Ma (Wells et al., 2014); and (2) the

Eocene Tyee Formation (Fm), which consists of a 3-km thick sequence of interbedded sand- and siltstones, representative of an expansive sequence of marine turbidites (Wells et al., 2014). Clockwise rotation of western Oregon since Tyee Fm deposition has placed the distal end of the Tyee ramp – where there is a higher proportion of siltstone – further north (Wells et al., 1998). Rock units generally young towards the northern OCR, ranging in age from the late Eocene to mid-Miocene, and are composed primarily of shallow marine sand- and siltstones that exhibit increased volcanic sediment inputs as Cascades volcanism initiated (Wells et al., 2014). Eocene-Oligocene igneous rocks (e.g., Tillamook Volcanics), including E-W striking dikes that criss-cross the OCR, outcrop locally and set local landscape morphology and sediment properties (Dietrich and Dunne, 1978; Sweeney et al., 2012; Wells et al., 2014). Finally, the Miocene Columbia River Basalts are present throughout much of the northern OCR, including as far south as the mouth of the Yaquina River (~44.6° N; Figure 1A). The Columbia River Basalts primarily outcrop near the present course of the Columbia River but also in the central WV, such as the Salem Hills, and throughout the Tualatin and Portland Basins near Portland, Oregon. Active crustal faults are common throughout the northern OCR and western margin of the WV (Wells et al., 2020).

The OCR exhibits relatively uniform relief, including steep, soil-mantled hillslopes that separate evenly spaced bedrock channels (Dietrich and Dunne, 1978). Soils are thinnest on hilltops (<0.5 m) and thicken towards unchannelized colluvial hollows (~1-2 m) and are produced and transported primarily by episodic bioturbation (Dietrich and Dunne, 1978; Roering et al., 2010). Soil production rates span a range from ~0.02 mm yr^{-1} on hillslopes with deep (~1 m) soils up to 0.268 mm yr^{-1} on hillslopes with thin to absent soils (Heimsath et al., 2001). Correspondingly, catchment-averaged erosion rates cluster at ~0.1 mm yr^{-1} (e.g., Heimsath et al., 2001; Penserini et al., 2017; Reneau and Dietrich, 1991), though these rates can vary spatially and temporally over glacial-interglacial timescales (Almond et al., 2007; Marshall et al., 2015; Struble and Roering, 2021). Uplift rates inferred from uplifted marine- and incised river terraces range from 0.05 mm yr^{-1} to >0.4 mm yr^{-1} (Kelsey et al., 1996; Personius, 1995). How far inland uplift rates determined from marine terraces extend is unclear, though Penserini et al. (2017) suggested an inboard increase in uplift rates based on the morphology of steepland valley networks. The consistency between catchment-averaged erosion rates and inferred uplift rates, as well as the relative spatial uniformity of erosion rates and soil production rates has led to the suggestion that the OCR is in steady state (Heimsath et al., 2001; Reneau and Dietrich, 1991). However, the range exhibits diverse hillslope and channel morphology that reflects lithologic controls on topographic form as well as expansive zones of stream capture and drainage reorganization (Almond et al., 2007; Baldwin and Howell, 1949; Struble et al., 2021; Struble and Roering, 2021). Bedrock landslides are morphologically distinct throughout the OCR and the margins of the CFL, apparent in topography as low-relief, "benchy" surfaces (Roering et al., 2005), and range in age from $<10^1$ to $>10^5$ yr (Balco et al., 2024; LaHusen et al., 2020). In the Tyee Fm, deep-seated landslides are more common in the northern siltstone-rich portions of the unit compared to the south where sandstone predominates (LaHusen and Grant, 2024; Roering et al., 2005).

The CFL is located on the eastern margin of the OCR and is bounded on the east by the Cascade volcanic arc. The CFL, in contrast to the steep and dissected OCR, exhibits broad and gentle hillslopes with intensely weathered, deep (>2 m) soils (Almond et al., 2007). These morphologically gentle hillslopes exhibit occasionally abrupt transitions to steep hillslopes of the OCR, often across shallow crustal faults (Wells et al., 2020; Yeats et al., 1996) and asymmetric drainage divides that have been proposed as locations of drainage reorganization (Baldwin and Howell, 1949; Struble et al., 2021). While there exist no previously published erosion rates for CFL-draining rivers, soil residence times often exceed 165 kyr (Almond et al., 2007), suggesting significantly slower erosion rates than the OCR. Away from the valley margins, the WV is characterized primarily by Quaternary fluvial terraces and flood deposits of the Willamette River and its tributaries as well as lacustrine silts emplaced during the Pleistocene Missoula Floods (O’Connor et al., 2001). Further south in the CFL, the Umpqua and Rogue Rivers exhibit similar fluvial deposits on incised strath terraces of Pleistocene age (Personius, 1993), though sedimentary fill is shallower and less extensive than the larger WV. The rocks of the CFL are generally the same as or lithologically similar to those at comparable latitudes in the OCR, though volcanic units from the Cascade Range predominate on the eastern margins of the lowland (Figure 1C). Long-term uplift (or subsidence) rates are generally poorly constrained throughout the CFL. However, the presence of sedimentary basins with basal sediments of Miocene to Quaternary age that are bounded by structures that separate the OCR and CFL suggest that the CFL is experiencing subsidence over Quaternary timescales and, at minimum, exhibits a stark contrast in uplift rate with the modern OCR (O’Connor et al., 2001; Wells et al., 2020).

The OCR and CFL experience warm, dry summers and cool, rainy winters. MAP approaches 5-m along portions of the coast and the highest elevations of the range, and there is an orographic precipitation gradient when moving eastward from the coast, such that much of the CFL receives <1-m of annual rainfall (Figure 1B; PRISM Climate Group, 2021). Vegetation consists primarily of Douglas-fir (*Pseudotsuga menziesii*) and western hemlock (*Tsuga heterophylla*) on the hillslopes, with red alder

(*Alnus rubra*), Oregon ash (*Fraxinus latifolia*), and Oregon maple (*Acer macrophyllum*) predominating in valley bottoms.

3. Methods

3.1 Hilltop curvature

To quantify controls on hillslope morphology across western Oregon, we downloaded ~42,824 km^2 of 1-m publicly available lidar data from the Oregon Department of Geological and Mineral Industries. This dataset includes the entirety of the OCR and western margin of the CFL as well as portions of the northern Klamath Mountains (Figure 1). At the time of analysis, lidar data had not yet been collected for most of the Klamath Mountains in far southwestern Oregon. After splitting the lidar data into 194 tiles ranging in size from ~53-528 km^2 (mean size of 221 km^2), we extracted channel and hilltop metrics using University of Oregon HPC facilities. Since defining channel networks is necessary to geometrically isolate the corresponding hilltops, we identified channel heads using the GeoNet method (Passalacqua et al., 2010) implemented in LSDTopoTools (Clubb et al., 2014; Mudd et al., 2021). This method involves filtering the digital elevation model (DEM) with a Perona-Malik filter before extracting channel heads with a tangential curvature threshold calculated from quantile-quantile plots of curvature across the DEM. We routed flow from channel heads to create a channel network with the Fastscape algorithm (Braun and Willett, 2013). We pruned the resulting network using a drainage area threshold of 2,000 m^2 to remove artificially small tributaries as well as single pixel channels. We then identified all hilltops at the intersection of drainage basin boundaries.

We calculated topographic curvature (Laplacian of elevation) by applying a 2-dimensional (2D) continuous wavelet transform (CWT) with a Ricker wavelet (Struble and Roering, 2021). The Ricker wavelet is the negative second derivative of a 2D Gaussian function and can be defined as

$$\psi(x,y) = \frac{1}{\pi s^4}\left(1 - \frac{(u-x)^2+(v-y)^2}{2s^2}\right)\exp\left[-\frac{(u-x)^2+(v-y)^2}{2s^2}\right], \tag{2}$$

where ψ is the wavelet function, (u,v) defines the location in space of ψ, and s is the size, or standard deviation, of the 2D Gaussian function from which ψ is derived. In order to avoid high-magnitude biases to curvature that are introduced by DEM noise and bioturbation (e.g., pit/mound topography), C_{HT} must be extracted from smoothed topography (Roering et al., 2010). Given the Ricker wavelet is the negative second derivative of a 2D Gaussian function (i.e., the Ricker wavelet is also a low-pass filter), s must be set to produce a scaled wavelet that smooths over these high-wavenumber artifacts. We utilized the definition of s for a wavelet that is the m^{th} derivative of a Gaussian (m=2 for the Ricker wavelet) given as

$$s = \frac{\lambda}{2\pi}\sqrt{m+\frac{1}{2}}, \tag{3}$$

where λ is the desired smoothing scale (Torrence and Compo, 1998). Previous work has shown that a smoothing scale of λ=15 m is appropriate for the OCR, based on the scale of pit-mound topography (i.e., tree throw pits) and topographic roughness ($s\approx3.77$ for 1-meter grid spacing; Roering et al., 2010). The 2D CWT is applied through a convolution ($*$ symbol) of ψ with topography, z, as

$$C(s,u,v) = z(x,y) * \psi\left(\frac{x-u}{s},\frac{y-v}{s}\right), \tag{4}$$

where C is the wavelet coefficient (curvature in this case). Equation 4 shows that curvature is dependent on topographic position (u and v) and wavelet scale (s). We used the resulting curvature rasters to extract C_{HT} along the mapped ridgelines.

To ensure that we only selected pixels representative of hilltops where sediment flux is linearly proportional to gradient (Roering et al., 2007), we removed pixels with a *hilltop* gradient (S_{HT})>0.4, pixels with positive C_{HT}, and pixels within 75 m of a mapped channel, which may represent or be influenced by concave areas of the landscape. We additionally utilized the landslide compilation from LaHusen et al. (2020) for the Tyee Fm and the state-wide Oregon landslide dataset SLIDO (Franczyk et al., 2019), to remove hilltops that fall within 100-m (a typical OCR hillslope length) of a mapped landslide. While high-resolution landslide databases for the OCR continue to grow, there exist few landslide compilations that have been mapped at the same resolution as the LaHusen et al. dataset outside of the Tyee Fm. As such, the SLIDO dataset is not yet a comprehensive dataset, and there are likely regions where we do not capture all landslides. Nevertheless, SLIDO identifies the largest landslides that are most likely to bias C_{HT}. We additionally utilized vector data of roads throughout Oregon to remove hilltops that fall within 30 m of mapped roads. In total, after trimming, we mapped 90,464,723 hilltop pixels throughout our study site. To visualize regional patterns in hillslope morphology, we gridded the C_{HT} data using a grid cell size of 1 km, taking the mean C_{HT} within each grid cell.

3.2 Erosion rates

We compiled existing cosmogenic ^{10}Be erosion rates for the OCR, emphasizing catchments within the Tyee Fm (Marshall et al., 2015; Penserini et al., 2017; Struble and Roering, 2021). We excluded erosion rates from watersheds that are sufficiently large to span long-wavelength variations in uplift and erosion rate, incorporate multiple lithologic units, or that have numerous deep-seated landslides. We additionally collected new ^{10}Be erosion rates for 11 watersheds in the Tyee Fm and lithologically similar adjacent units (Eocene-Oligocene age Fisher and Eugene Fms), emphasizing catchments in the eastern OCR and western WV, where gentle hillslopes and broad alluvial valleys morphologically suggest a slower erosion rate. We collected stream sediments that exhibited signs of recent fluvial transport, and we avoided catchments with significant sediment cover in the valley bottoms that would suggest prolonged sediment storage. Assuming that erosion has been steady over the ^{10}Be accumulation timescale and is equally averaged over the whole upstream drainage area, we calculated erosion rates with CRONUS v3 (Balco et al., 2008). We additionally recalculated previously published erosion rates in CRONUS to ensure consistent calculation of erosion rate from measured ^{10}Be concentrations across the complete dataset. ^{10}Be concentrations and erosion rates can be found in Table 1. We compared our mapped catchment-averaged C_{HT} to erosion rate across these 18 watersheds.

3.3 Climate and lithological datasets

In order to explore non-tectonic controls on the spatial distribution of C_{HT}, we compiled regional-scale climate and lithology datasets. We estimated MAP across the region using the 30-year averaged precipitation data from 1991-2020 (PRISM Climate Group, 2021). These data have a grid resolution of 800-m; the spatial distribution of MAP across the region can be seen in Figure 1B.

To constrain the impact of lithology on C_{HT}, we analyzed geological data from the Oregon Geologic Data Compilation (Smith and Roe, 2015). These data represent the most complete geologic map data for the state, integrating 346 source maps, and include 101 different geological formations within our study region. To enable us to determine regional trends, we grouped these units into 13 broader lithological categories, aiming to preserve potential erodibility contrasts (for example, separating mudstones from sandstones and conglomerates), but without introducing an excessive number of units that obfuscates any potential trends with C_{HT}. We separated out different marine sedimentary units as they are the most spatially extensive lithologies across the study region. These lithological categories and their spatial distribution can be seen in Figure 1C. We performed a pairwise Kolmogorov-Smirnov (K-S) test on the distribution of C_{HT} in each lithological category, which tests the null hypothesis that each pair of samples came from the same underlying distribution. We found that the distribution of C_{HT} was significantly distinct ($p<0.05$) for each lithology, suggesting that our categories adequately capture differences in C_{HT} between lithologies (Figure S1). We then combined the lithology and MAP data with our gridded C_{HT} dataset, calculating the average precipitation (mm yr^{-1}) and lithological group of each 1 km^2 grid cell.

4 Results

We compared catchment-averaged C_{HT} to measured erosion rates from cosmogenic ^{10}Be (Table 1). We observed a significant linear relationship between erosion rate and C_{HT} (Figure 3; $E=1.12*C_{HT}$, $R^2=0.88$, $p<0.0001$). Erosion rates fall into approximately two populations, corresponding to slowly eroding catchments along the margins of the WV and the more rapidly eroding core of the OCR. Based on Equation 1 and assuming $\frac{\rho_s}{\rho_r} = 0.5$, the regression line between erosion rate and C_{HT} implies a hillslope diffusivity of D=0.0022 $m^2\ yr^{-1}$.

We observed regional-scale variations in C_{HT} throughout the Cascadia forearc. Notably, swath profiles illustrate that C_{HT} is high in the core of the OCR (i.e., sharper hilltops) and decays eastwards towards the CFL (Figure 4), producing a long-wavelength signal in C_{HT}. Given the linear relationship we observed between erosion rate and C_{HT} (Figure 3), our results suggest that hillslopes in the CFL are eroding at least ~3-4 times slower than the OCR.

There also exists variability in C_{HT} *within* the OCR that does not appear to solely reflect baselevel. Specifically, we observed that C_{HT} varies with the dominant underlying lithology in the Cascadia forearc. For instance, in the northern OCR, we observed spatially that the Tillamook Volcanics exhibit systematically sharper hilltops than surrounding regions composed primarily of marine mud- and siltstones (Figure 4). Similarly, much of the Tyee Fm exhibits elevated C_{HT} compared to lithologically similar units to the north and south. However, even *within* the Tyee Fm, C_{HT} is generally high further south and decays northwards (compare swaths 3 and 4 in Figure 4). More broadly, igneous and metamorphic units like the basaltic rocks of Siletzia, the Tillamook Volcanics, and the northern Klamath Mountains exhibit larger C_{HT} than many sedimentary units, with the exception of marine sedimentary and turbidite rocks, which includes the Tyee Fm (Figure 5). Mean C_{HT} is lowest in terrestrial sedimentary rocks and unconsolidated sediments. This may be a reflection, in part, of the predominance of these units in the slowly eroding CFL relative to the steeper OCR, where such units are absent, as well as due to the likely high transport efficiency, D, of unconsolidated sediments in general. Mapped terrestrial sedimentary rocks and unconsolidated sediments include incised deposits of the Willamette River and ancient Columbia River (O'Connor et al., 2001).

We additionally observed that C_{HT} may exhibit a positive relationship with MAP (Figure 6). As noted in Section 2, there are significant variations in lithology between the northern and southern OCR, which may obscure any climatic influence on C_{HT}. Therefore, we plotted the relationship between MAP and C_{HT} separated into 0.5° latitude bins, preserving the E-W precipitation gradient whilst removing some lithologic complexity. Figure 6 shows there is a positive relationship between MAP and C_{HT} for most latitude bins north of 43°N, although there is also variability within the dataset which may be linked to variations in geomorphic process or lithology within each latitude bin or covariation between MAP and lithology or uplift rate. The latitudes representing the "core" of the OCR (43-44°N), primarily made up of the Tyee Fm, show the clearest positive relationship between MAP and C_{HT}. However, C_{HT} reaches a maximum at intermediate precipitation rates of ~2000 mm yr^{-1} within these latitudes and then decreases at higher MAP. There is no relationship between MAP and C_{HT} in the southern OCR, despite a wide range in MAP.

5 Discussion

5.1 Controls on C_{HT}

We observed a linear relationship between C_{HT} and catchment-average erosion rates measured with ^{10}Be (Figure 3). While C_{HT} exhibits a clear linear relationship with erosion rate, this observation does not, by itself, implicate tectonic or climatic control on hillslope form (i.e., climatic variability impacts steady state C_{HT} through diffusivity; Equation 1). However, the distribution of C_{HT} throughout western Oregon suggests that tectonics is the predominant control on baselevel, which ultimately sets C_{HT}. We consider the relative contributions of tectonics, climate, and lithology to C_{HT} below.

We observed that C_{HT} in western Oregon exhibits long-wavelength variability between the OCR and CFL that is largely a reflection of tectonically-controlled baselevel lowering rate (Figure 3). Specifically, the magnitude of C_{HT} is systematically greater in the rapidly eroding OCR and grades into the adjacent slowly eroding CFL (Figure 4). This long-wavelength pattern in C_{HT} mirrors observations that the CFL spans the length of the Cascadia Subduction Zone, past the southern drainage divide of the WV into the Umpqua and Rogue drainage basins (Struble et al., 2021). If the regional, long-wavelength topography of the OCR and CFL is reflective of tectonic processes (Bomberger et al., 2018; Struble et al., 2021), then the long-wavelength variability we observed in C_{HT} suggests a predominately tectonic control on baselevel and C_{HT} throughout western Oregon. Furthermore, we noted conspicuous abrupt transitions of C_{HT} across mapped structures that bound the OCR and CFL, including the Glenbrook Fault near the drainage divide between the Siuslaw and Willamette Rivers (Figure 7; Yeats et al., 1996), which mirror similarly abrupt contrasts in soil weathering and residence time (Almond et al., 2007). Lithology and MAP remain consistent across these structures, thus supporting a strong uplift control on baselevel and hillslope morphology. Furthermore, sedimentary basins in the WV are often sufficiently deep to have contacts between late Miocene to Quaternary-age unconsolidated sedimentary units and older bedrock units below sea-level, indicative of WV subsidence over Quaternary timescales (O'Connor et al., 2001; Wells et al., 2020). Some of these basins are several kilometers deep, and many of the basin-bounding faults are active (Wells et al., 2020; Yeats et al., 1996). In addition, observations of positive and negative "dynamic" topography in the OCR and CFL, respectively, suggest relative variations in uplift rate that set baselevel throughout the forearc (Becker et al., 2014). Finally, while there exist no independent measurements of uplift rate in the OCR or CFL (i.e., from thermochronology), Penserini et al. (2017) suggested an increase in uplift rate towards the core of the OCR based on differences between interseismic and long-term uplift rates inferred from the morphology of steepland valleys. We similarly observed the largest values of C_{HT} in the core of the OCR that taper towards the coast and CFL (Figure 4).

For the case of climatic control on C_{HT}, we observed that, when separated by latitude, there is some correlation between C_{HT} and MAP, though there is significant scatter in the relationship (Figure 6). Such a correlation inspires several possible interpretations. If MAP does control C_{HT}, high precipitation rates may drive rapid fluvial baselevel lowering rates that produce steeper hillslopes and sharper hilltops (Ferrier et al., 2013), particularly if increased vegetation supported by high MAP allows for steeper slopes (Perron, 2017). Similarly, increased precipitation may produce more frequent or larger debris flows that force the hilltop to sharpen (Stock and Dietrich, 2006; Struble et al., 2023). Alternatively, the literature-favored impact of climate on hillslope morphology states that higher MAP results in increased hillslope sediment transport efficiency (higher D in Equation 1), producing gentler hillslopes and broader hilltops for a given erosion rate (Perron, 2017; Richardson et al., 2019). However, this is the opposite of what we observed (Figure 6). Importantly, the OCR exhibits a pronounced orographic precipitation gradient, such that, in some places, the western OCR exhibits MAP >3 times that of the eastern OCR and CFL (Figure 1B). This orographic precipitation gradient mirrors the long-wavelength form of the OCR (Figures 1B, 4). In other words, where uplift rate is likely rapid in the OCR core, MAP is similarly high. Furthermore, in latitude bins where we observed correlation between C_{HT} and MAP, these relationships are often not monotonic. Specifically, while we observed a positive correlation at some latitudes between C_{HT} and MAP for MAP <1-~2 m yr^{-1}, this relationship breaks down at MAP >~2 m yr^{-1} where there is no correlation, or even a negative correlation, between C_{HT} and MAP (Figure 6). Furthermore, the southern OCR (42 - 43°N) does not show a clear relationship between MAP and C_{HT}, despite having a similar precipitation gradient to the northern OCR (Figure 1B, 6). Hence, we interpret that the increase in C_{HT} with MAP in the central and northern OCR is indeed likely linked to broad co-variation of uplift and MAP – or perhaps even covariation between uplift and lithology wherein erosionally resistant rocks are at the core of the OCR – rather than climate acting as a dominant control on hilltop morphology.

Superimposed on the long-wavelength pattern in C_{HT}, we observed that lithology influences C_{HT}. Quaternary sedimentary units, for instance, tend to exhibit gentle broad hilltops while hilltops underlain by marine sedimentary and volcanic rocks are generally sharp (Figure 5). Importantly, however, swath profile 3 in Figure 4 illustrates that the long-wavelength C_{HT} pattern across the OCR and CFL remains apparent even when isolating observations to only the Tyee Fm, suggesting that this long-wavelength pattern does not arise due to a systematic lithologic contrast between the OCR and CFL. Furthermore, there is a wide range of C_{HT} that corresponds to only the Tyee Fm (Figure 8, S2). Similarly, the distributions of C_{HT} for separate lithologies in Figure 5 show that each lithologic unit nearly spans the full range of C_{HT} values (Figure S2). As such, lithology alone cannot explain the systematic variations in C_{HT} that we observed, and we interpret lithology as having a secondary control on hillslope form.

The second-order influence of lithology on C_{HT} may reflect variable soil transport and production rates due to disparate chemical and physical weathering and soil disturbance processes. For instance, within the Tyee Fm, C_{HT} is generally higher in the south (swath 3 in Figure 4) and decays northward (swath 2 in Figure 4). While this northward decrease in C_{HT} may imply a concomitant decrease in erosion rate, it may also spatially correspond to the higher proportion of siltstone to sandstone in the northern Tyee Fm compared to further south and imply that within-formation rock properties may influence the soil production and transport processes that set hilltop convexity. In addition, lidar often qualitatively reveals topographic variations that coincide with lithologic contacts, although the mechanisms that underlie these patterns are not well understood. While the pace of soil production and transport has been proposed to vary systematically with climate variables (Amundson et al., 2015; Perron, 2017), few studies have assessed how lithologic variation affects model parameters. For example, if soil production depends on lithology (Johnstone and Hilley, 2015) and transport follows a depth-dependent relationship (Roering, 2008), lithologic boundaries should coincide with changes in hilltop convexity all else equal. These feedbacks on hillslope form have yet to be thoroughly tested and evidence supporting more complex curvature-erosion relationships is limited. Importantly, for the results we present here, the catchments where we have erosion rate data are at similar latitudes within the Tyee Fm (Figure 1A), implying that north-south variations in sandstone-siltstone concentration do not systematically affect our observed relationship between erosion rate and C_{HT} (Figure 3). We cannot rule out, however, that there may be a less pronounced east-west lithologic variability that may introduce scatter to our observed E-C_{HT} relationship (LaHusen and Grant, 2024; Roering et al., 2005).

Taken together, quantitative uncertainties about the spatial distribution of uplift rate throughout the OCR make explicitly deconvolving the precise relative contributions of tectonics, climate, and lithology to hillslope form in the OCR and CFL an acute challenge and beyond the scope of this work. However, the long-wavelength variation in C_{HT} throughout the forearc coupled with abrupt contrasts across mapped – and often active – faults that likely separate disparate baselevel lowering rates, suggests that tectonics sets baselevel lowering rate and, by extension, C_{HT} throughout the Oregon forearc. MAP, in contrast, likely covaries with uplift rate and exhibits a secondary control on hilltop morphology, as does lithologic heterogeneity. These results are consistent with past observations that note that hillslope morphology is set primarily by baselevel, while lithology exerts a secondary role though soil production variability and sediment transport (Hurst et al., 2013; Johnstone and Hilley, 2015).

5.2 Nature of relationship between erosion rate and C_{HT}

We observed a robust, linear relationship between erosion rate and C_{HT} (Figure 3). While there is increased scatter in curvature values at more rapid erosion rates, we did not observe consistently lower-than-expected values that would suggest that C_{HT} approaches a threshold value or that the relationship is less-than-linear. Fitting a power-law to the E-C_{HT} relationship does not produce an improved fit. We interpret this in one of several possible ways. Firstly, our observations may fully reflect a theoretically-predicted linear relationship between erosion rate and C_{HT} that is valid across most natural soil-mantled landscapes (Equation 1; Roering et al., 2007). While this is possible, it does not explicitly address observations made by others that compiled datasets of C_{HT} approximate a square-root relationship (Gabet et al., 2021). Struble and Roering (2021) suggested that square-root relationships may emerge when landscapes with conspicuously fast erosion rates produce hilltops that are sufficiently narrow such that planar sideslopes abut hilltops. In these cases, curvature measurement windows incorporate these near-zero curvatures, since smoothing scales cannot be made sufficiently small to capture ridgeline-scale curvature, as topographic roughness remains high at the smallest scales. In other words, *there is no single smoothing scale that can simultaneously smooth over DEM noise and roughness and capture the* *underlying C_{HT} of conspicuously sharp and narrow hilltops*. The erosion rate at which this systematic underestimation becomes relevant depends on diffusivity; small diffusivities result in underestimation at slower erosion rates (Struble and Roering, 2021). For the diffusivities inferred in the OCR (D=0.0022-0.003 m^2 yr^{-1} based on Figure 3 and previous analyses), and for λ=15 m, systematic underestimation of C_{HT} (in this case, an underestimate of the *actual* value by 10%) is not expected until erosion rates approach or exceed 0.2 mm yr^{-1} (Figure 11 in Struble and Roering, 2021). As such, the OCR, or at least the portion of the OCR where erosion rates have been independently measured with ^{10}Be, may be eroding sufficiently slow such that systematic underestimation is not significant, given that the most rapid erosion rates we observed are <0.15 mm yr^{-1}. We note, however, that the erosion rates at which C_{HT} is expected to be underestimated were determined from synthetic hillslopes *without* added topographic noise (Struble and Roering, 2021). As such, natural hillslopes with erosion rates less than those noted by Struble and Roering (2021) may exhibit systematic deviations from a linear relationship between process and form. Further work is necessary to characterize the spectral properties of topographic roughness of soil-mantled hillslopes and how natural roughness, across a range of landscapes, may be systematically used to inform the selection of λ as well as process-based explanations for nonlinear relationships between erosion rate and C_{HT}. Furthermore, in some landscapes where the erosion rate exceeds the soil production rate, C_{HT} decouples from erosion rate as the hillslope is stripped of its soil mantle (Heimsath et al., 2012). It is ambiguous, however, whether there exists a range of erosion rates at which hilltop curvature remains coupled to erosion rate, even as soils become patchy, or if progressive decoupling of C_{HT} and erosion rate at rapid erosion rate is indicative of a transiently thinning soil mantle or a soil mantle that is becoming spatially patchy.

5.3 Computational efficiency of the CWT promotes regional analyses

Our analysis highlights the utility of the CWT for mapping C_{HT} across regional scales due to the ability of the CWT to rapidly calculate curvature while simultaneously acting as a low-pass filter. Struble and Roering (2021) observed that the CWT often operates 10^3 times faster than other techniques for calculating curvature. For the case of λ=15 m, which is the smoothing scale we use here, the CWT operates *at least* 10^2 times faster than past approaches for relatively small DEMs (their largest test DEM was 682x682 meters, or ~0.47 km^2; Struble and Roering, 2021). Given we used larger DEMs for this analysis (up to 528 km^2), we tested the computational speed of the CWT and a 2D polynomial, both with λ=15 m, on a DEM tile that spanned ~153 km^2, which is smaller than our mean DEM size. We found that the CWT ran in 11.2 seconds, while the polynomial took 79.7 *minutes*, corresponding to a computational advantage of ~427. For larger DEMs, this computational advantage is even greater. As such, we emphasize that the CWT presents an exciting opportunity for pursuing regional-scale geomorphic analyses that link topographic form to surface processes with high-resolution lidar data, including more explicitly linking hilltops to downstream fluvial and debris-flow channels (e.g., Clubb et al., 2020; Godard et al., 2020; Grieve et al., 2016; Struble et al., 2023). In addition, C_{HT} can be measured locally and indicates local baselevel lowering rate and sediment transport efficiency. While sediment transport efficiency, or diffusivity, may spatially vary throughout a landscape or fluctuate through time (Marshall et al., 2015), regional-scale measurements of C_{HT} allow for regional mapping of diffusivity, so long as erosion rate can be independently constrained. As such, regional C_{HT} analyses will allow for continued examination of the tectonic, climatic, lithologic, and biologic controls on C_{HT}, the scaling relationship between C_{HT} and erosion rate and, by extension, diffusivity, as well as interrogation of topographic roughness and noise that informs the selection of appropriate topographic smoothing scales (Gabet et al., 2021; Struble and Roering, 2021).

Conclusions

We utilized continuous wavelet transforms (CWTs) to map hilltop curvature, C_{HT}, throughout western Oregon, constituting analysis of ~43,000 km^2 of 1-meter lidar data. The speed of the CWT to calculate curvature, compared to other commonly used curvature measurement techniques, facilitates regional scale analyses. We observed that C_{HT} exhibits a linear relationship with erosion rate, as measured from cosmogenic ^{10}Be for a portion of the Oregon Coast Range (OCR) where lithology is relatively uniform. Throughout the Cascadia forearc, the magnitude of C_{HT} is larger (sharper hilltops) in the OCR than in the Cascadia Forearc Lowland (CFL), which includes the Willamette Valley. This observation suggests an uplifting core of the Oregon Coast Range that is eroding 3-4 times faster than the CFL. We additionally noted that lithology exerts a secondary impact on C_{HT}, with volcanic rocks and sandstone members of the turbidite-rich Tyee Formation underlying sharper hilltops. In contrast, silt- and mudstones and Quaternary-age unconsolidated sediments exhibit the broadest, gentlest hilltops, which likely reflect the rapid pace of sediment transport and soil production (high diffusivity) for these lithologic units, but also the collocation of Quaternary units in slowly eroding regions like the CFL. We observed a nonmonotonic relationship between C_{HT} and mean annual precipitation (MAP), likely reflecting covariation between uplift and MAP in the forearc, though sparse quantitative datasets of uplift prohibit explicit testing of this covariation. Regardless, long-wavelength variability in C_{HT} across the forearc that mirrors the development of tectonically-produced landforms, namely deep sedimentary basins, suggests that tectonics is the predominant control on baselevel and hillslope morphology in the OCR and CFL, with lithology and climate playing secondary roles.

Our results highlight the applicability of CWTs for measuring C_{HT} over regional scales, an ability that was heretofore impractical due to slow curvature computation times and a general dearth of high-resolution topographic data. While future studies will require careful analyses that avoid curvature biases introduced by landslides and anthropogenic impacts (e.g., roads, buildings), regional mapping of C_{HT} opens the door to improving understanding of linkages between tectonics and surface processes, climatic and biologic impacts on landscape morphology, soil production, and biogeochemical processes, including soil organic carbon storage.

Acknowledgements and Data Availability

This work was supported in part by a University of Oregon Lokey Doctoral Fellowship to W.T.S. We thank Iris Vineyards, Pfeiffer Winery, RainSong Vineyard, and Aprovecho Research Center for facilitating field access for collecting erosion rate data. Annette Patton, Brooke Hunter, Jerod Aguilar, and Ryan Brown helped collect ^{10}Be erosion rate samples in the field. This paper also greatly benefitted from reviews by Tyler Doane and an anonymous reviewer. ^{10}Be data were processed at Lawrence Livermore National Laboratory. Lidar data are publicly available from the Oregon Department of Geology and Mineral Industries (DOGAMI, https://www.oregon.gov/dogami/lidar/Pages/index.aspx). Vector data used to trim hilltops mapped on or near roads are publicly accessible from the USGS National Transportation Dataset (NTD) for Oregon (https://www.sciencebase.gov/catalog/item/5a61c939e4b06e28e9c3bdab). MATLAB code used to

calculate hilltop curvature can be found at https://github.com/wtstruble/HilltopCurvature_Wavelets, and TopoToolbox is available at https://topotoolbox.wordpress.com. We calculated erosion rates using CRONUS v3, available at https://hess.ess.washington.edu/. This work benefited from access to the University of Oregon high performance computer, Talapas.

CRediT author contributions

William T. Struble: Conceptualization, data curation, formal analysis, funding acquisition, investigation, methodology, software, visualization, writing-original draft, writing-review & editing.

Fiona J. Clubb: Data curation, formal analysis, investigation, methodology, software, visualization, writing-original draft, writing-review & editing.

Joshua J. Roering: Conceptualization, funding acquisition, investigation, writing-review & editing.

References

Adams, B.A., Whipple, K.X., Forte, A.M., Heimsath, A.M., Hodges, K.V., 2020. Climate controls on erosion in tectonically active landscapes. Sci. Adv. 6, eaaz3166. https://doi.org/10.1126/sciadv.aaz3166

Almond, P., Roering, J., Hales, T.C., 2007. Using soil residence time to delineate spatial and temporal patterns of transient landscape response. Journal of Geophysical Research 112. https://doi.org/10.1029/2006JF000568

Amundson, R., Heimsath, A., Owen, J., Yoo, K., Dietrich, W.E., 2015. Hillslope soils and vegetation. Geomorphology 234, 122–132. https://doi.org/10.1016/j.geomorph.2014.12.031

Balco, G., Hidy, A., Struble, W.T., Roering, J.J., 2024. Short Communication: Cosmogenic noble gas depletion in soils by wildfire heating. Geochronology 6, 71–76. https://doi.org/10.5194/gchron-6-71-2024

Balco, G., Stone, J.O., Lifton, N.A., Dunai, T.J., 2008. A complete and easily accessible means of calculating surface exposure ages or erosion rates from 10Be and 26Al measurements. Quaternary Geochronology 3, 174–195. https://doi.org/10.1016/j.quageo.2007.12.001

Baldwin, E.M., Howell, P.W., 1949. The Long Tom, a Former Tributary of the Siuslaw River. Northwest Science 23, 112–124.

Becker, T.W., Faccenna, C., Humphreys, E.D., Lowry, A.R., Miller, M.S., 2014. Static and dynamic support of western United States topography. Earth and Planetary Science Letters 402, 234–246. https://doi.org/10.1016/j.epsl.2013.10.012

Bomberger, C., Bendick, R., Flesch, L., Ehlers, T.A., 2018. Spatial Scales in Topography and Strain Rate Magnitude in the Western United States. Journal of Geophysical Research: Solid Earth 123, 6086–6097. https://doi.org/10.1029/2018JB016135

Braun, J., Willett, S.D., 2013. A very efficient O(n), implicit and parallel method to solve the stream power equation governing fluvial incision and landscape evolution. Geomorphology 180–181, 170–179. https://doi.org/10.1016/j.geomorph.2012.10.008

Clubb, F.J., Mudd, S.M., Hurst, M.D., Grieve, S.W.D., 2020. Differences in channel and hillslope geometry record a migrating uplift wave at the Mendocino triple junction, California, USA. Geology 48, 184–188. https://doi.org/10.1130/G46939.1

Clubb, F.J., Mudd, S.M., Milodowski, D.T., Hurst, M.D., Slater, L.J., 2014. Objective extraction of channel heads from high-resolution topographic data. Water Resour. Res. 50, 4283–4304. https://doi.org/10.1002/2013WR015167

Culling, W.E.H., 1963. Soil creep and the development of hillside slopes. Journal of Geology 71, 127–161.

Deshpande, N., Furbish, D., Arratia, P., Jerolmack, D., 2021. The perpetual fragility of creeping hillslopes. Nature Communications 12. https://doi.org/10.1038/s41467-021-23979-z

DiBiase, R.A., Whipple, K.X., Heimsath, A.M., Ouimet, W.B., 2010. Landscape form and millennial erosion rates in the San Gabriel Mountains, CA. Earth and Planetary Science Letters 289, 134–144. https://doi.org/10.1016/j.epsl.2009.10.036

Dietrich, W.E., Bellugi, D.G., Sklar, L.S., Stock, J.D., Heimsath, A.M., Roering, J.J., 2003. Geomorphic transport laws for predicting landscape form and dynamics, in: Wilcock, P.R., Iverson, R.M. (Eds.), Geophysical Monograph Series. American Geophysical Union, Washington, D. C., pp. 103–132.

Dietrich, W.E., Dunne, T., 1978. Sediment budget for a small catchment in mountainous terrain. Zeitschrift für Geomorphologie N.F. 29, 191–206. https://doi.org/10.1007/s10069-002-0008-0

Dixon, J.L., Heimsath, A.M., Kaste, J., Amundson, R., 2009. Climate-driven processes of hillslope weathering. Geology 37, 975–978. https://doi.org/10.1130/G30045A.1

Ferrier, K.L., Huppert, K.L., Perron, J.T., 2013. Climatic control of bedrock river incision. Nature 496, 206–209. https://doi.org/10.1038/nature11982

Franczyk, J.J., Burns, W.J., Calhoun, N.C., 2019. Statewide Landslide Information Database for Oregon Release-4.0, SLIDO 4.0, Digital Data Series. Oregon Department of Geology and Mineral Industries.

Gabet, E.J., Mudd, S.M., Wood, R.W., Grieve, S.W.D., Binnie, S.A., Dunai, T.J., 2021. Hilltop Curvature Increases With the Square Root of Erosion Rate. JGR Earth Surface 126. https://doi.org/10.1029/2020JF005858

Gilbert, G.K., 1877. Report on the Geology of the Henry Mountains. US Government Printing Office.

Godard, V., Hippolyte, J.-C., Cushing, E., Espurt, N., Fleury, J., Bellier, O., Ollivier, V., the ASTER Team, 2020. Hillslope denudation and morphologic response to a rock uplift gradient. Earth Surf. Dynam. 8, 221–243. https://doi.org/10.5194/esurf-8-221-2020

Grieve, S.W.D., Mudd, S.M., Milodowski, D.T., Clubb, F.J., Furbish, D.J., 2016. How does grid-resolution modulate the topographic expression of geomorphic processes? Earth Surface Dynamics 4, 627–653. https://doi.org/10.5194/esurf-4-627-2016

Heimsath, A.M., DiBiase, R.A., Whipple, K.X., 2012. Soil production limits and the transition to bedrock-dominated landscapes. Nature Geosci 5, 210–214. https://doi.org/10.1038/ngeo1380

Heimsath, A.M., Dietrich, W.E., Kunihiko, N., Finkel, R.C., 1997. The soil production function and landscape equilibrium. Nature 388, 358–361.

Heimsath, A.M., Dietrich, W.E., Nishiizumi, K., Finkel, R.C., 2001. Stochastic processes of soil production and transport: erosion rates, topographic variation and cosmogenic nuclides in the Oregon Coast Range. Earth Surface Processes and Landforms 26, 531–552. https://doi.org/10.1002/esp.209

Hunter, B.D., Roering, J.J., Silva, L.C.R., Moreland, K.C., 2024. Geomorphic controls on the abundance and persistence of soil organic carbon pools in erosional landscapes. Nat. Geosci. https://doi.org/10.1038/s41561-023-01365-2

Hurst, M.D., Mudd, S.M., Walcott, R., Attal, M., Yoo, K., 2012. Using hilltop curvature to derive the spatial distribution of erosion rates. Journal of Geophysical Research: Earth Surface 117, 1–19. https://doi.org/10.1029/2011JF002057

Hurst, M.D., Mudd, S.M., Yoo, K., Attal, M., Walcott, R., 2013. Influence of lithology on hillslope morphology and response to tectonic forcing in the northern Sierra Nevada of California. J. Geophys. Res. Earth Surf. 118, 832–851. https://doi.org/10.1002/jgrf.20049

Johnstone, S.A., Hilley, G.E., 2015. Lithologic control on the form of soil-mantled hillslopes. Geology 43, 83–86. https://doi.org/10.1130/G36052.1

Kelsey, H.M., Ticknor, R.L., Bockheim, J.G., Mitchell, E., 1996. Quaternary upper plate deformation in coastal Oregon. Geological Society of America Bulletin 108, 843–860. https://doi.org/10.1130/0016-7606(1996)108%3C0843:QUPDIC%3E2.3.CO;2

Kirby, E., Whipple, K., 2001. Quantifying differential rock-uplift rates via stream profile analysis. Geology 29, 415–418.

LaHusen, S.R., Duvall, A.R., Booth, A.M., Grant, A., Mishkin, B.A., Montgomery, D.R., Struble, W., Roering, J.J., Wartman, J., 2020. Rainfall triggers more deep-seated landslides than Cascadia earthquakes in the Oregon Coast Range, USA. Sci. Adv. 6, eaba6790. https://doi.org/10.1126/sciadv.aba6790

LaHusen, S.R., Grant, A.R.R., 2024. Complex landslide patterns explained by local intra-unit variability of stratigraphy and structure: Case study in the Tyee Formation, Oregon, USA. Engineering Geology 329, 107387. https://doi.org/10.1016/j.enggeo.2023.107387

Lai, L.S., Roering, J.J., Finnegan, N.J., Dorsey, R.J., Yen, J., 2021. Coarse sediment supply sets the slope of bedrock channels in rapidly uplifting terrain: Field and topographic evidence from eastern Taiwan. Earth Surf Processes Landf 46, 2671–2689. https://doi.org/10.1002/esp.5200

Larsen, I.J., Montgomery, D.R., 2012. Landslide erosion coupled to tectonics and river incision. Nature Geoscience 5, 468–473. https://doi.org/10.1038/ngeo1479

Marshall, J.A., Roering, J.J., Bartlein, P.J., Gavin, D.G., Granger, D.E., Rempel, A.W., Praskievicz, S.J., Hales, T.C., 2015. Frost for the trees: Did climate increase erosion in unglaciated

landscapes during the late Pleistocene? Science Advances 1, e1500715–e1500715. https://doi.org/10.1126/sciadv.1500715
Moon, S., Perron, J.T., Martel, S.J., Holbrook, W.S., St. Clair, J., 2017. A model of three-dimensional topographic stresses with implications for bedrock fractures, surface processes, and landscape evolution. J. Geophys. Res. Earth Surf. 122, 823–846. https://doi.org/10.1002/2016JF004155
Mudd, S.M., Clubb, F.J., Grieve, S.W.D., Milodowski, D.T., Gailleton, B., Hurst, M.D., Valters, D.V., Wickert, A.D., Hutton, E.W.H., 2021. LSDTopoTools2 v0.5.
Mudd, S.M., Furbish, D.J., 2005. Lateral migration of hillcrests in response to channel incision in soil-mantled landscapes. Journal of Geophysical Research: Earth Surface 110. https://doi.org/10.1029/2005JF000313
O'Connor, J.E., Sarna-Wojcicki, A., Wozniak, K.C., Polette, D.J., Fleck, R.J. (Eds.), 2001. Origin, extent, and thickness of Quaternary geologic units in the Willamette Valley, Oregon, U.S. Geological Survey professional paper. U.S. Dept. of the Interior, U.S. Geological Survey ; For sale by the U.S. Geological Survey, Information Services, Reston, Va. : Denver, CO.
Passalacqua, P., Do Trung, T., Foufoula-Georgiou, E., Sapiro, G., Dietrich, W.E., 2010. A geometric framework for channel network extraction from lidar: Nonlinear diffusion and geodesic paths. Journal of Geophysical Research 115. https://doi.org/10.1029/2009JF001254
Penserini, B.D., Roering, J.J., Streig, A., 2017. A morphologic proxy for debris flow erosion with application to the earthquake deformation cycle, Cascadia Subduction Zone, USA. Geomorphology 282, 150–161. https://doi.org/10.1016/j.geomorph.2017.01.018
Perron, J.T., 2017. Climate and the Pace of Erosional Landscape Evolution.
Personius, S.F., 1995. Late Quaternary stream incision and uplift in the forearc of the Cascadia subduction zone, western Oregon. Journal of Geophysical Research: Solid Earth 100, 20193–20210. https://doi.org/10.1029/95JB01684
Personius, S.F., 1993. Age and origin of fluvial terraces in the central Coast Range, western Oregon (U.S. Geological Survey Bulletin No. 2038). United States Geological Survey, United States Government Printing Office, Washington. https://doi.org/10.3133/b2038
Piotraschke, R., Cashman, S.M., Furlong, K.P., Kamp, P.J.J., Danišík, M., Xu, G., 2015. Unroofing the Klamaths—Blame it on Siletzia? Lithosphere 7, 427–440. https://doi.org/10.1130/L418.1
PRISM Climate Group, 2021. PRISM Climate Group: Oregon State University.
Reneau, S.L., Dietrich, W.E., 1991. Erosion rates in the southern Oregon Coast Range: Evidence for an equilibrium between hillslope erosion and sediment yield. Earth Surface Processes and Landforms 16, 307–322.
Richardson, P.W., Perron, J.T., Schurr, N.D., 2019. Influences of climate and life on hillslope sediment transport. Geology. https://doi.org/10.1130/G45305.1
Roering, J.J., 2008. How well can hillslope evolution models "explain" topography? Simulating soil transport and production with high-resolution topographic data. Geological Society of America Bulletin 120, 1248–1262. https://doi.org/10.1130/B26283.1
Roering, J.J., Kirchner, J.W., Dietrich, W.E., 2005. Characterizing structural and lithologic controls on deep-seated landsliding: Implications for topographic relief and landscape evolution in the Oregon Coast Range, USA. Geological Society of America Bulletin 117, 654. https://doi.org/10.1130/B25567.1

Roering, J.J., Kirchner, J.W., Dietrich, W.E., 1999. Evidence for nonlinear, diffusive sediment transport on hillslopes and implications for landscape morphology. Water Resources Research 35, 853–870.

Roering, J.J., Marshall, J., Booth, A.M., Mort, M., Jin, Q., 2010. Evidence for biotic controls on topography and soil production. Earth and Planetary Science Letters 298, 183–190. https://doi.org/10.1016/j.epsl.2010.07.040

Roering, J.J., Perron, J.T., Kirchner, J.W., 2007. Functional relationships between denudation and hillslope form and relief. Earth and Planetary Science Letters 264, 245–258. https://doi.org/10.1016/j.epsl.2007.09.035

Scherler, D., Schwanghart, W., 2020. Drainage divide networks – Part 1: Identification and ordering in digital elevation models. Earth Surf. Dynam. 8, 245–259. https://doi.org/10.5194/esurf-8-245-2020

Smith, R.L., Roe, W.P., 2015. OGDC-6, Oregon Geologic Data Compilation, release 6.

Stock, J.D., Dietrich, W.E., 2006. Erosion of steepland valleys by debris flows. Geological Society of America Bulletin 118, 1125–1148.

Struble, W.T., McGuire, L.A., McCoy, S.W., Barnhart, K.R., Marc, O., 2023. Debris-Flow Process Controls on Steepland Morphology in the San Gabriel Mountains, California. JGR Earth Surface 128, e2022JF007017. https://doi.org/10.1029/2022JF007017

Struble, W.T., Roering, J.J., 2021. Hilltop curvature as a proxy for erosion rate: Wavelets enable rapid computation and reveal systematic underestimation. Earth Surface Dynamics 9, 1279–1300. https://doi.org/10.5194/esurf-9-1279-2021

Struble, W.T., Roering, J.J., Dorsey, R.J., Bendick, R., 2021. Characteristic Scales of Drainage Reorganization in Cascadia. Geophys Res Lett 48. https://doi.org/10.1029/2020GL091413

Sweeney, K.E., Roering, J.J., Almond, P., Reckling, T., 2012. How steady are steady-state landscapes? Using visible–near-infrared soil spectroscopy to quantify erosional variability. Geology 40, 807–810. https://doi.org/10.1130/G33167.1

Sweeney, K.E., Roering, J.J., Ellis, C., 2015. Experimental evidence for hillslope control of landscape scale. Science 349, 51–53. https://doi.org/10.1126/science.aab0017

Torrence, C., Compo, G.P., 1998. A Practical Guide to Wavelet Analysis. Bulletin of the American Meteorological Society 79, 18.

Walker, G.W., Duncan, R.A., 1989. Geologic map of the Salem 1 degree x 2 degrees, quadrangle, western Oregon.

Wells, R., Bukry, D., Friedman, R., Pyle, D., Duncan, R., Haeussler, P., Wooden, J., 2014. Geologic history of Siletzia, a large igneous province in the Oregon and Washington Coast Range: Correlation to the geomagnetic polarity time scale and implications for a long-lived Yellowstone hotspot. Geosphere 10, 692–719. https://doi.org/10.1130/GES01018.1

Wells, R.E., Blakely, R.J., Bemis, S., 2020. Northward migration of the Oregon forearc on the Gales Creek fault. Geosphere 16, 660–684. https://doi.org/10.1130/GES02177.1

Wells, R.E., Weaver, C.S., Blakely, R.J., 1998. Fore-arc migration in Cascadia and its neotectonic significance. Geology 26, 759–762.

Willett, S.D., McCoy, S.W., Perron, J.T., Goren, L., Chen, C.-Y., 2014. Dynamic Reorganization of River Basins. Science 343, 1248765–1248765. https://doi.org/10.1126/science.1248765

Yeats, R.S., Graven, E.P., Werner, K.S., Goldfinger, C., Popowski, T.A., 1996. Tectonics of the Willamette Valley, Oregon. US Government Printing Office.

Sample Name	Location (°N, °W)	Elevation (m)	^{10}Be Concentration (atoms g^{-1} quartz)	Error (atoms g^{-1} quartz)	Erosion Rate (mm yr^{-1})	Error (mm yr^{-1})	Notes
BattleCreek	43.951183, -123.326674	168	147493	3171.20	0.022	0.00183	This study
SwingLog2	43.934768, -123.342266	283	222345	4260.15	0.0157	0.0013	This study
SwingLog3	43.935489, -123.343606	287	340199	6796.70	0.00998	0.000838	This study
Iris	43.878106, -123.257832	255	270665	5389.93	0.0124	0.00103	This study
LowPass	44.195327, -123.421841	232	110772	2219.14	0.0316	0.0026	This study
Alderwood	44.154822, -123.422672	168	121650	2432.09	0.0271	0.00223	This study
Pfeiffer	44.236118, -123.3651	152	253101	4471.15	0.0122	0.00101	This study
TipCreek	43.779098, -123.315006	317	272895	5255.17	0.013	0.00108	This study
SiuslawFalls	43.854584, -123.364656	171	156311	2788.81	0.0207	0.00117	This study
Aprovecho	43.846, -123.13	374	262844	7005.15	0.0142	0.00121	This study
PutnamValley	43.648, -123.411	325	50398	1017.12	0.077	0.00631	This study
Trib 1	44.16343, -123.60448	450	53800	7300	0.10	0.01	Marshall et al. (2015)
Bear Creek	44.186231, -123.374644	213	400359	7974.33	0.00783	0.000663	Struble and Roering (2021)
Hadsall	43.98549, -123.82431	279	33766	4666.26	0.113	0.018	Penserini et al. (2017)
NFSR	43.963796, -123.810745	413	70903	3408.59	0.058	0.0054	Penserini et al. (2017)
Sullivan-North	43.470123, -124.105632	296	53212	22369.24	0.071	0.0305	Penserini et al. (2017)
Sullivan-South	43.468451, -124.103682	272	56074	5376.31	0.066	0.00824	Penserini et al. (2017)
Franklin	43.669592, -123.905054	294	44164	2592.00	0.0862	0.00851	Penserini et al. (2017)

Table 1: Sample sites for cosmogenic ^{10}Be erosion rates from quartz sand. Note that all for all samples, it was assumed that density was 2.65 g/cm^3 and topographic shielding was negligible. All samples were processed with 07KNSTD AMS standardization and non-time-dependent scaling for spallogenic production. Sample Name, if not new to this study, is that of the originally published name.

Figures

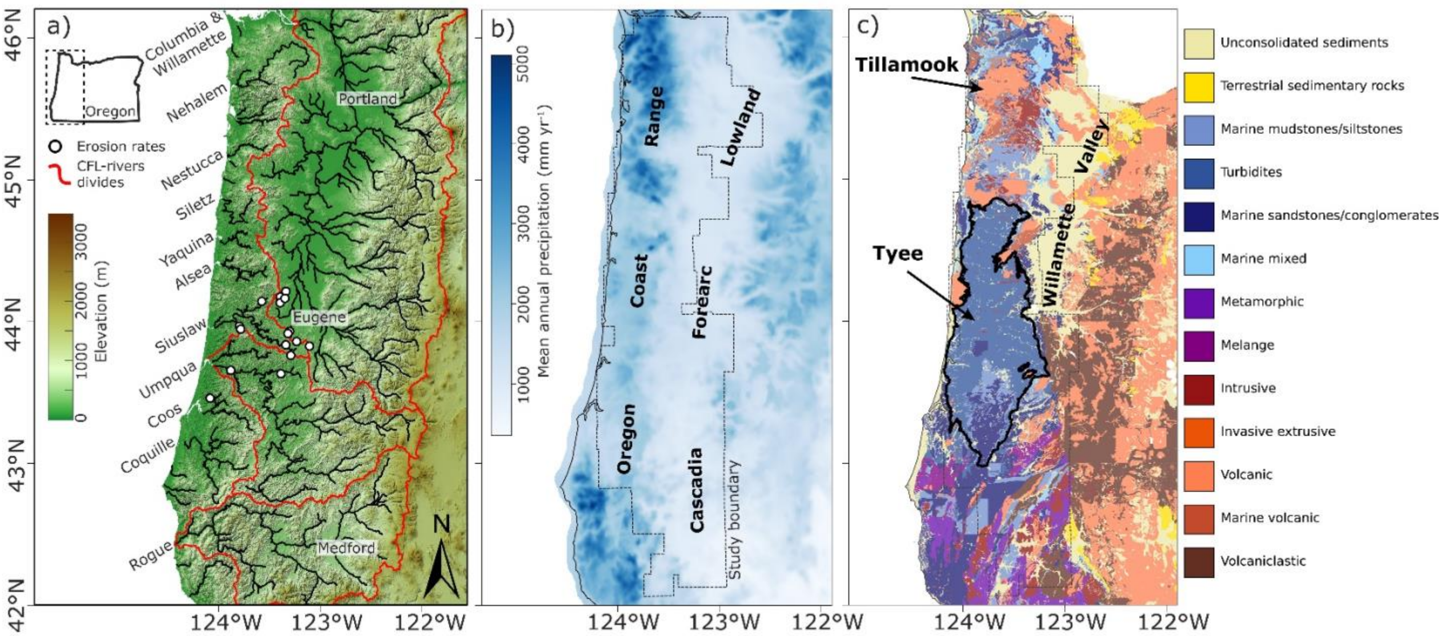

Figure 1: Western Oregon study site. A) Major rivers of western Oregon, with CFL-draining rivers (Willamette, Umpqua, Rogue) drainage basin outlines in red. Catchment-averaged erosion rate sample sites are shown by white circles. B) Mean annual precipitation (MAP) for western Oregon. Note the much drier CFL. The boundary for the lidar DEMs are shown by the dashed line. At the time of analysis, lidar for most of the Klamath Mountains in far southwestern Oregon was unavailable. C) Separated lithologic units utilized for comparison to C_{HT}. Tyee Formation is outlined in black and Tillamook Volcanics are labeled. See text for details of lithologic unit separation.

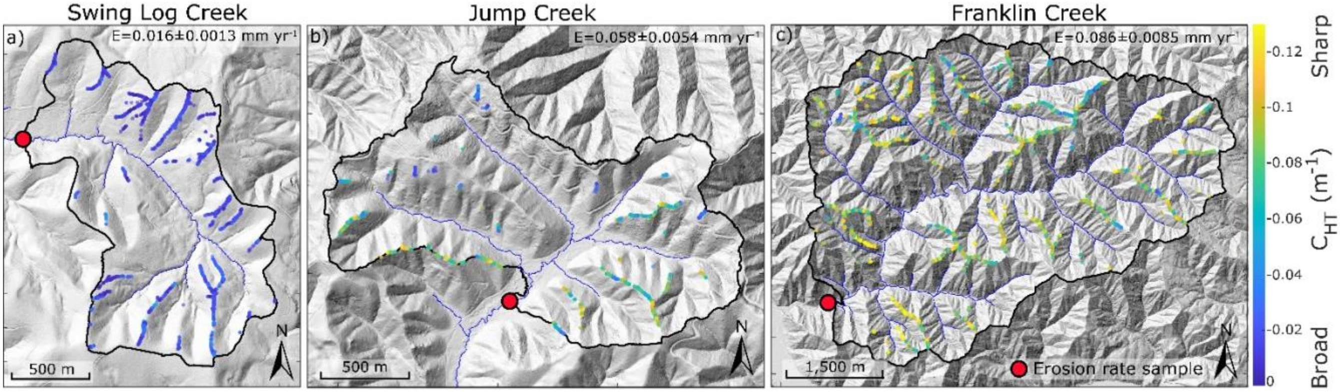

Figure 2: Example of mapped hilltops colored by measured C_{HT} at slow (Swing Log Creek; ^{10}Be sample SwingLog2), moderate (Jump Creek), and fast (Franklin Creek) erosion rates. Red dots correspond to erosion rate sample locations.

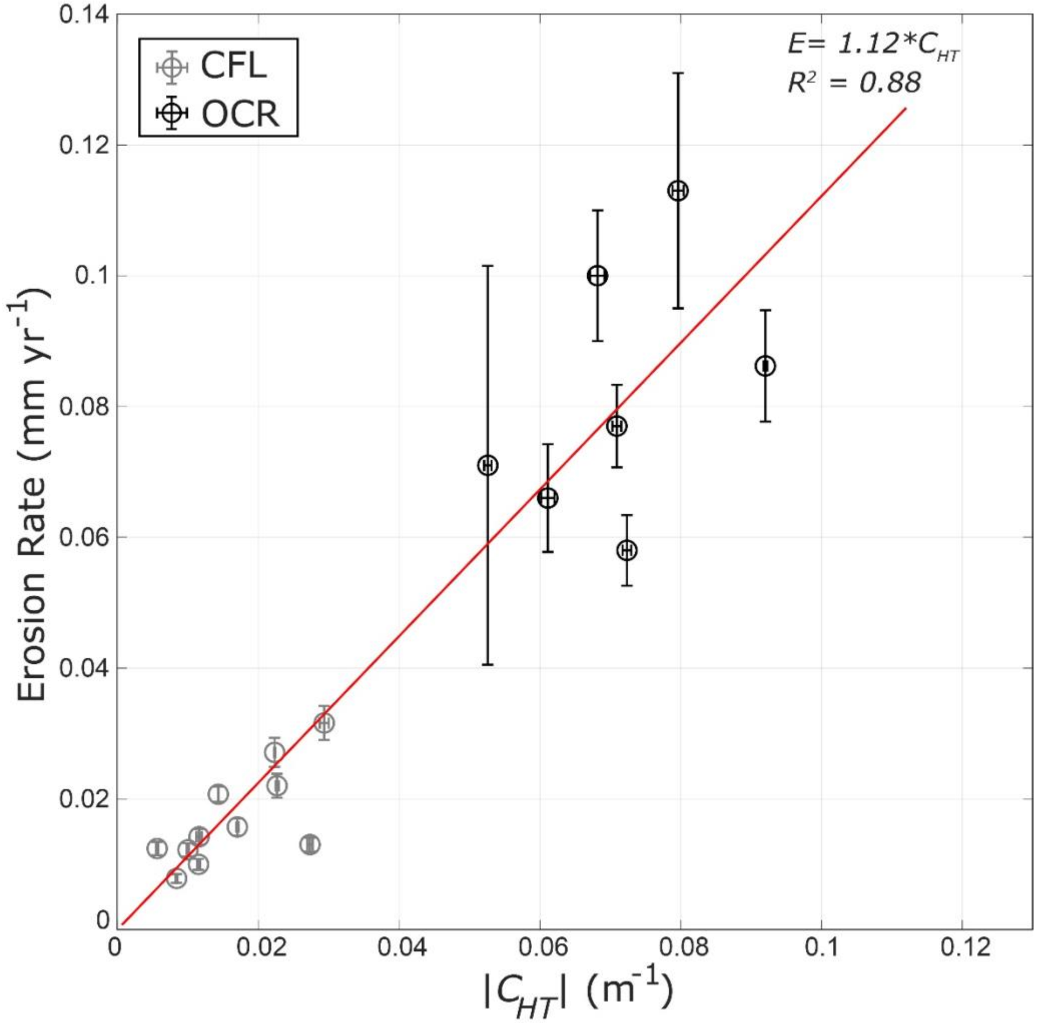

Figure 3: There exists a statistically significant (p<0.0001) linear relationship between catchment-averaged erosion rate measured with ^{10}Be and $|C_{HT}|$. The population of slow erosion rates and gentle hilltops correspond with catchments within or on the margins of the CFL (gray) whereas the fast-eroding sites correspond with the core of the OCR (black).

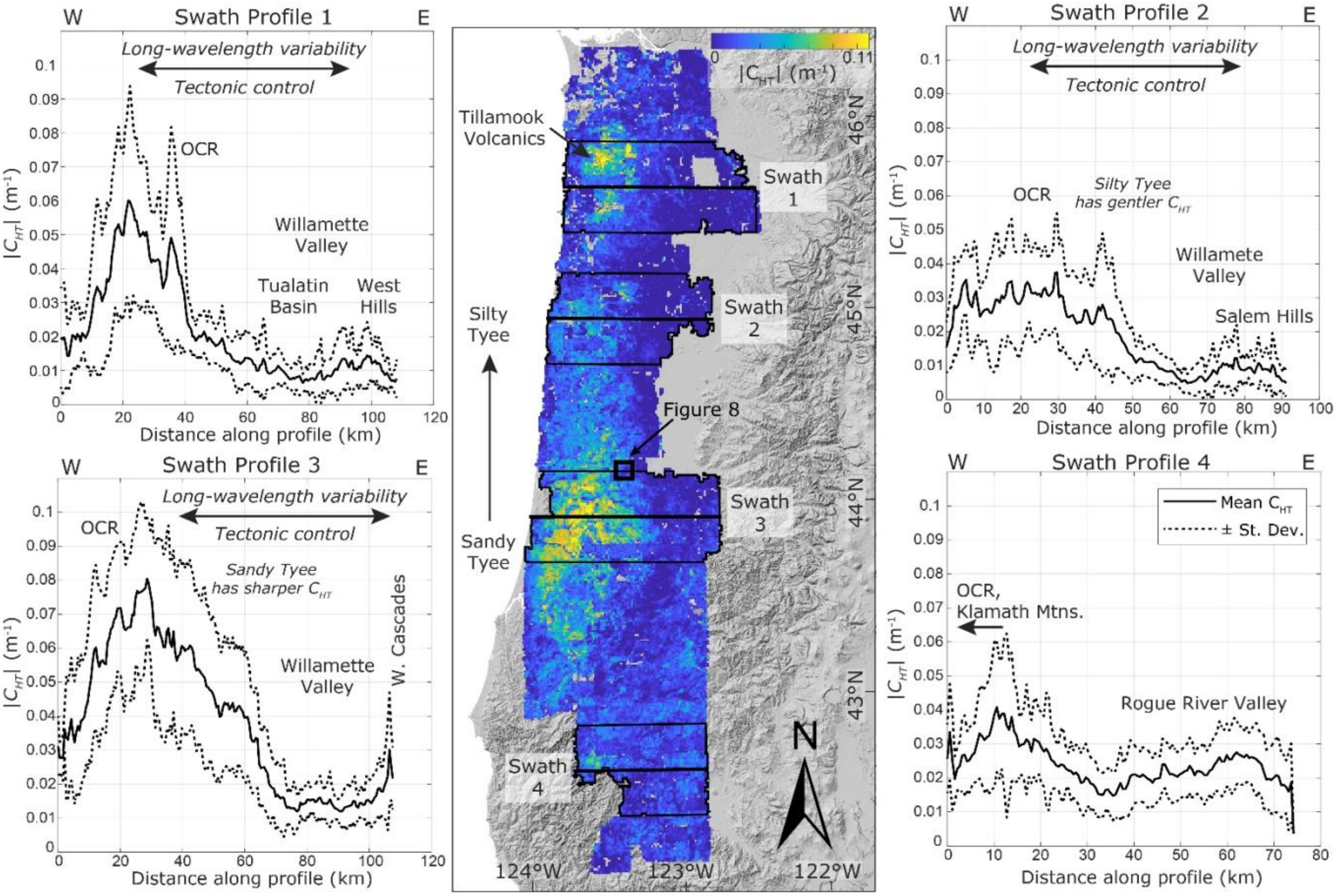

Figure 4: Map of 1-km^2 gridded C_{HT} in the OCR and CFL with West-to-East swath profiles, with major landforms labeled. In each swath profile, long-wavelength variability in C_{HT} highlights contrasts between the OCR and CFL and emphasizes tectonic, baselevel control on C_{HT}. See text for other interpretations. Note that swath 4 does not include the majority of the steep Klamath Mountains (likely large C_{HT}) as lidar data did not exist for this region at the time of analysis. Patchy gaps in gridded data correspond with regions where spatially expansive landslides were clipped or where larger sedimentary basins were excluded.

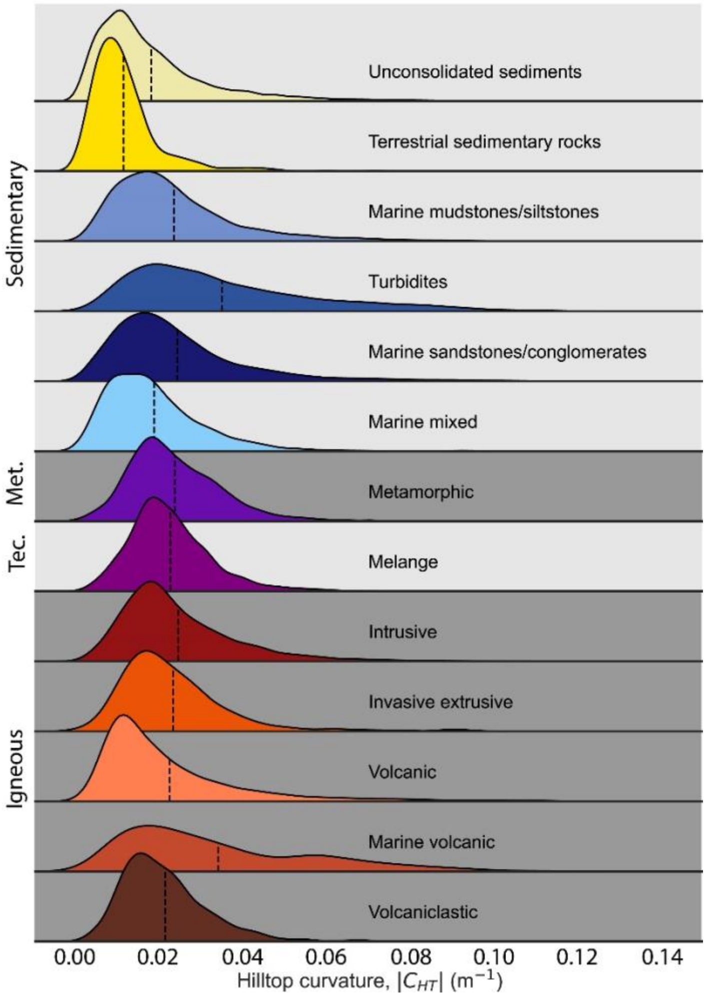

Figure 5: Kernel density functions of C_{HT} corresponding to mapped lithologic units in the forearc. Mean values plotted as dashed lines. Unconsolidated sediments and terrestrial sedimentary rocks exhibit the gentlest slopes (mostly Willamette Valley Quaternary sediments). Igneous rocks tend to exhibit the sharpest hilltops, although turbidite units, largely corresponding to the Tyee Formation, also exhibit sharp hilltops and have a heavy-tailed distribution.

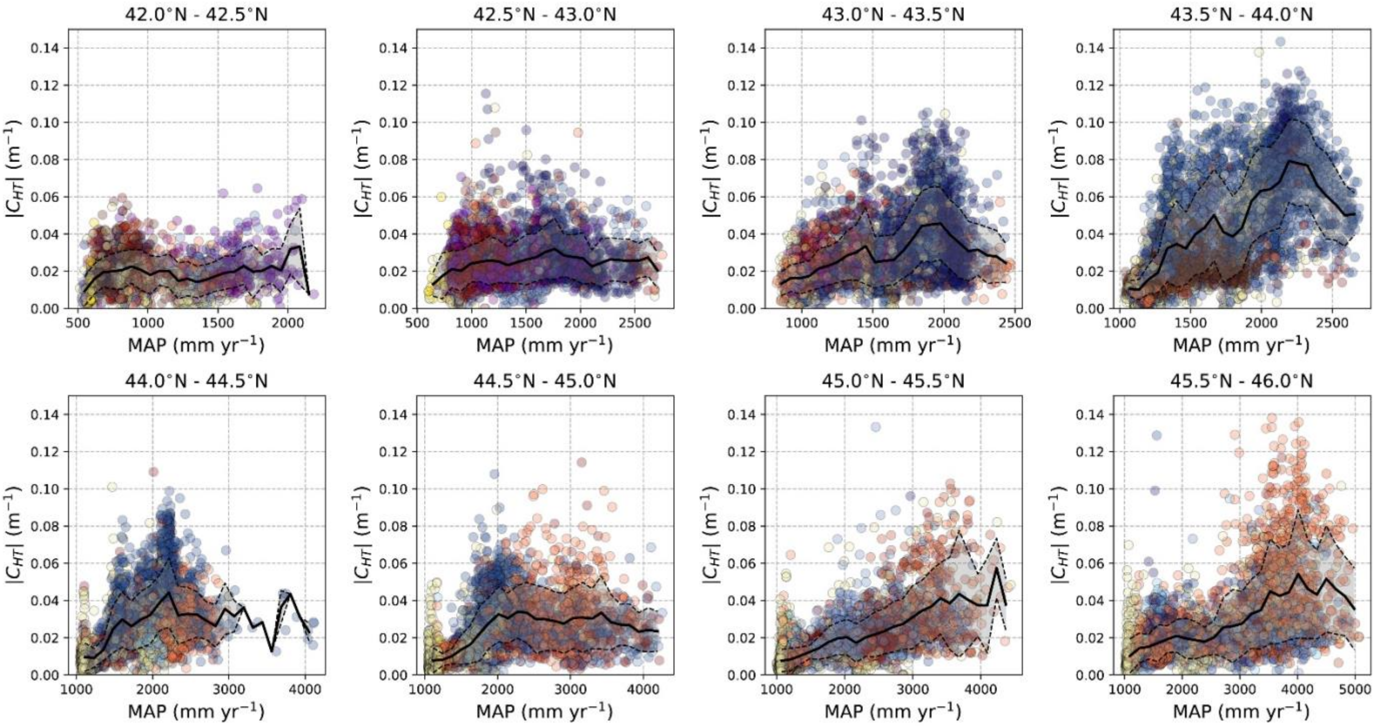

Figure 6: C_{HT} plotted against MAP separated by latitude. Points are colored by lithologic unit (see legend in Figure 1C). Note lack of correlation between C_{HT} and MAP at southern latitudes (42°N-43°N). In the central OCR (43.5°N-44.0°N), there exists a positive correlation between C_{HT} and MAP at low to moderate MAP. This relationship becomes a negative correlation at high MAP (>~2,200 mm yr^{-1}), likely highlighting the influence of orography on MAP (and thus covariation between uplift and MAP). Solid and dashed lines correspond to moving means and standard deviations.

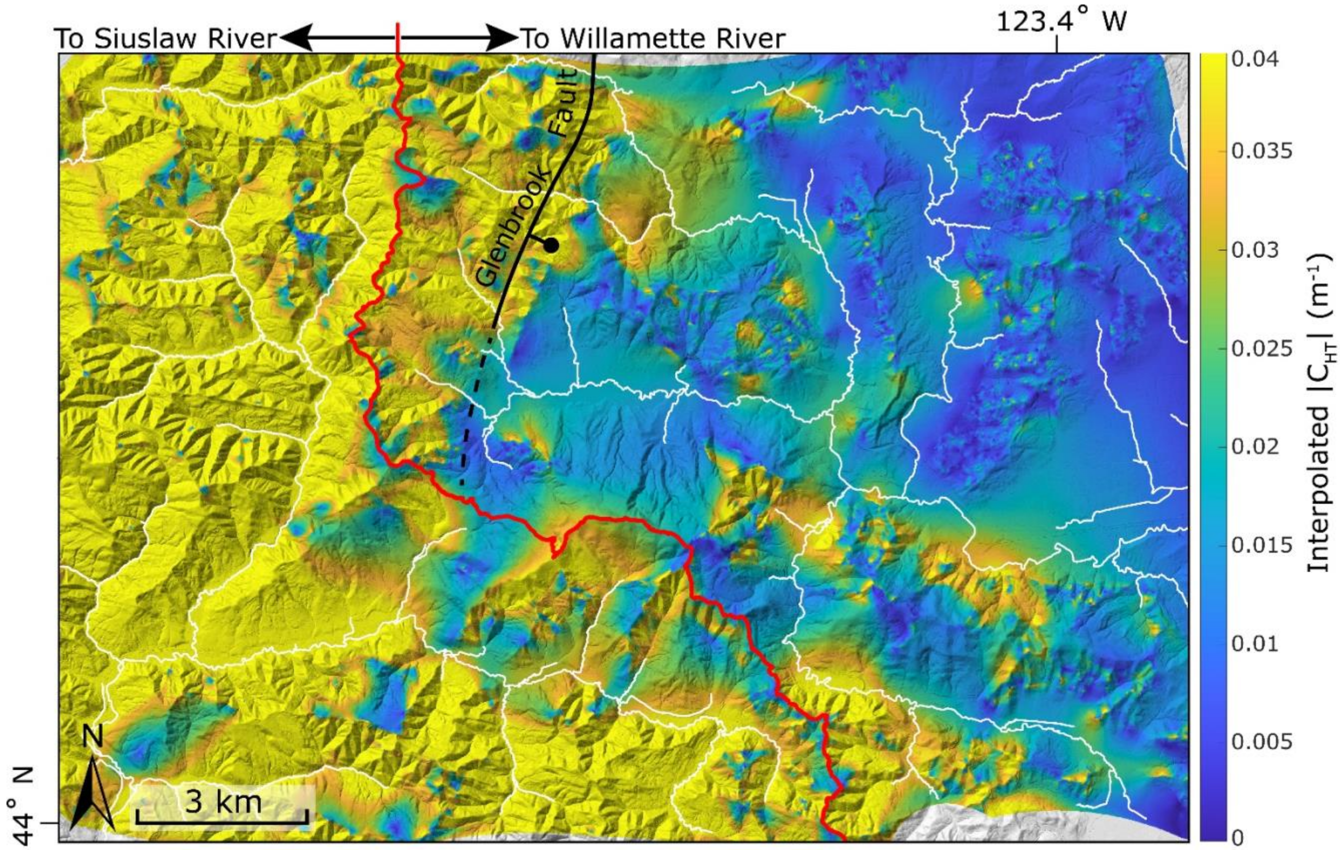

Figure 7: Natural neighbor interpolated C_{HT} proximal to the drainage divide (red line) between Siuslaw and Willamette Rivers (see black box in Figure 4 for location). Glenbrook Fault is mapped with the eastern block downthrown, dashed where inferred (based on Walker and Duncan, 1989). Tyee Formation is mapped on both sides of the fault. C_{HT} is lower in the Willamette drainage basin to the east of the fault and exhibits a sharp contrast near the fault. Drainage network shown by white line.

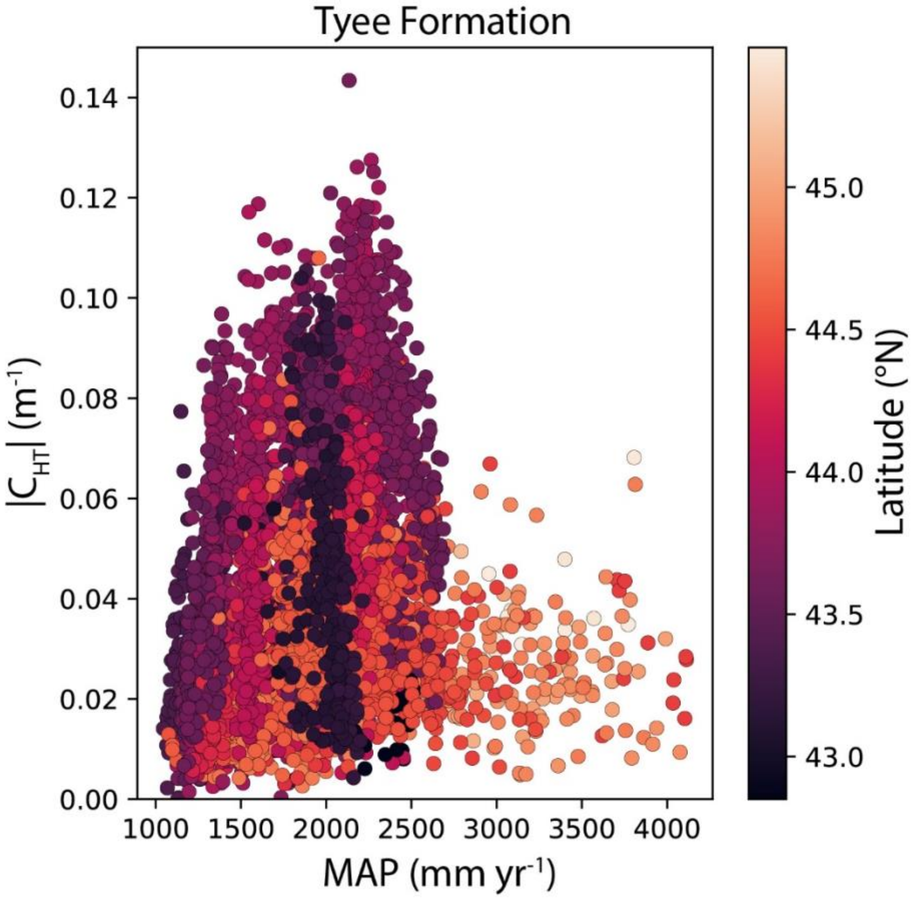

Figure 8: C_{HT} plotted against MAP for the Tyee Fm. Points are colored by latitude. Note wide range of C_{HT} values for similar MAP, especially at MAP<~2500 mm yr^{-1}, and for latitudes south of ~44°N. Note the generally smaller C_{HT} for the northern Tyee Fm where there is a greater proportion of weaker siltstone beds.